ADVANCED MATERIALS
www.advmat.de

Terahertz Nonlinear Hall Rectifiers Based on Spin-Polarized Topological Electronic States in 1T-$CoTe_2$

Zhen Hu, Libo Zhang, Atasi Chakraborty, Gianluca D'Olimpio, Jun Fujii, Anping Ge, Yuanchen Zhou, Changlong Liu, Amit Agarwal, Ivana Vobornik, Daniel Farias, Chia-Nung Kuo, Chin Shan Lue, Antonio Politano, Shao-Wei Wang, Weida Hu, Xiaoshuang Chen, Wei Lu, and Lin Wang**

The zero-magnetic-field nonlinear Hall effect (NLHE) refers to the second-order transverse current induced by an applied alternating electric field; it indicates the topological properties of inversion-symmetry-breaking crystals. Despite several studies on the NLHE induced by the Berry-curvature dipole in Weyl semimetals, the direct current conversion by rectification is limited to very low driving frequencies and cryogenic temperatures. The nonlinear photoresponse generated by the NLHE at room temperature can be useful for numerous applications in communication, sensing, and photodetection across a high bandwidth. In this study, observations of the second-order NLHE in type-II Dirac semimetal $CoTe_2$ under time-reversal symmetry are reported. This is determined by the disorder-induced extrinsic contribution on the broken-inversion-symmetry surface and room-temperature terahertz rectification without the need for semiconductor junctions or bias voltage. It is shown that remarkable photoresponsivity over 0.1 A W^{-1}, a response time of approximately 710 ns, and a mean noise equivalent power of 1 pW $Hz^{-1/2}$ can be achieved at room temperature. The results open a new pathway for low-energy photon harvesting via nonlinear rectification induced by the NLHE in strongly spin–orbit-coupled and inversion-symmetry-breaking systems, promising a considerable impact in the field of infrared/terahertz photonics.

1. Introduction

The rising interest in topological semimetals marks a new paradigm of research beyond the early landmarks of band-structure engineering in crystalline solids.[1] To date, a variety of topological semimetals have been explored that have hosted multiple excitations of quasiparticles, such as Dirac, Weyl, and exotic novel fermions, which originate from versatile symmetry breaking in condensed-matter systems.[2] Without Lorenz invariance, topologically protected type-II Dirac/Weyl semimetals, where Dirac cones are strongly tilted along a specific momentum direction, provide unique electronic and optical properties. Some examples highlighting the geometry and topological properties of Bloch wave functions are nonlinear optical effects,[3] anisotropic magnetotransport, and chiral anomalies.[4]

Significant efforts have been devoted to the optical control of the structural and

Z. Hu, L. Zhang, A. Ge, Y. Zhou, S.-W. Wang, W. Hu, X. Chen, W. Lu, L. Wang
State Key Laboratory of Infrared Physics
Shanghai Institute of Technical Physics
Chinese Academy of Sciences
500 Yu-tian Road, Shanghai 200083, China
E-mail: wanglin@mail.sitp.ac.cn

Z. Hu, A. Ge, S.-W. Wang, W. Hu, X. Chen, W. Lu, L. Wang
University of Chinese Academy of Sciences
No. 19A Yuquan Road, Beijing 100049, China

L. Zhang, C. Liu, W. Hu, X. Chen
College of Physics and Optoelectronic Engineering
Hangzhou Institute for Advanced Study
University of Chinese Academy of Sciences
No. 1, Sub-Lane Xiangshan, Xihu District, Hangzhou 310024, China

The ORCID identification number(s) for the author(s) of this article can be found under https://doi.org/10.1002/adma.202209557.

DOI: 10.1002/adma.202209557

A. Chakraborty, A. Agarwal
Department of Physics
Indian Institute of Technology Kanpur
Kanpur 208016, India

G. D'Olimpio, A. Politano
Department of Physical and Chemical Sciences
University of L'Aquila
via Vetoio, (AQ), 67100 L'Aquila, Italy
E-mail: antonio.politano@univaq.it

J. Fujii, I. Vobornik
Consiglio Nazionale delle Ricerche (CNR)- Istituto Officina dei Materiali (IOM)
Laboratorio TASC in Area Science
Park S.S. 14 km 163.5, 34149 Trieste, Italy

D. Farias
Departamento de Física de la Materia Condensada and Instituto "Nicolás Cabrera"
Universidad Autónoma de Madrid
28049 Madrid, Spain

D. Farias
Condensed Matter Physics Center (IFIMAC)
Universidad Autónoma de Madrid
28049 Madrid, Spain

electronic properties of topological semimetals via nonlinear responses by photoexcitation, such as high-order harmonic generation,[5] light frequency mixing,[6] and Floquet engineering.[7] These open new possibilities for the development of dissipationless and ultrafast topological devices in data processing, sensing, and communication.[8] Therefore, photodetectors exploiting different light-induced effects have recently been explored, including orbital-selective photoexcitation,[9] large quantized circular photogalvanic effect,[10] and spatial dispersive circulating photocurrent effect,[11] leading to a significant injection/shift current contribution in the mid-infrared regime. The substantial enhancement of the generated photocurrent was ascribed to the strong nonlinear effects associated with the geometric properties of the Bloch bands and the singularities of the Berry flux field at the Weyl nodes.

Despite the aforementioned advantages, photodetection is limited by the low photon energy range of the terahertz (THz) band, which is approximately 0.1–10 THz, because of considerable drawbacks imposed by weak optical absorption, high dark current, and inefficient charge-separation mechanisms.[12] While a divergent shift current response is expected owing to the geometrical effects of type-II WSM in the low-frequency $\omega \to 0$ limits, the optical injection of chiral carriers in Weyl cones can be mitigated out by the thermal agitation noise or Pauli-blocking effect at room temperature.[13] In addition, conventional thermal- and photon-type photodetectors for low-energy photon detection are limited by low speed, cryogenic cooling, and high power requirement. Therefore, the development of high-performance photodetectors that performs well at room temperature remains challenging.[14]

A recent study revealed a large THz anomalous Hall conductivity in Mn_3Sn, making it a WSM candidate with noncollinear antiferromagnetic ordering.[15] The large THz anomalous Hall effect induced by the intrinsic Berry curvature with time-reversal symmetry breaking suggests the possibility of field-controlling Weyl nodes in the alternating change (AC) regime.[15b] Unlike the linear AC Hall effect, which disappears in time-reversal invariant systems, the second-order nonlinear Hall effect (NLHE) has emerged as a highly intriguing response that relies only on the broken inversion symmetry of quantum materials.[16] A new member of the Hall effect, the NLHE can generate a direct current owing to the rectification of the driving alternating current in the absence of a magnetic field. This was observed in time-reversal invariant Weyl semimetal T_d-WTe_2 and $TaIrTe_4$, revealing the geometric nature driven by the intrinsic Berry curvature dipole.[17] In addition, the second-order NLHE can be driven by extrinsic contributions, namely skew scattering and side jump mechanisms, to the broken-inversion-symmetry topological surface state, thus providing a potential means to generate a considerable second-order nonlinear effect with topological bands.[18] Beyond the fundamental interest in the exploration of large NLHE at THz frequencies at room temperature, overcoming the problems of conventional THz photodetectors is promising. Specifically, the NLHE can enable a full-wave "Hall rectifier" governed by intrinsic quantum effects.[19] Thus, investigating emerging topological materials with strong spin–orbit coupling and related NLHEs could lead to possible applications of high-frequency rectifiers in the THz regime.

In this study, we demonstrate the presence of second-order NLHE in a 1T-$CoTe_2$ crystal hosting strongly spin-polarized topological surface states and type-II Dirac fermions in the bulk, as detected by spin- and angle-resolved photoelectron spectroscopy (spin-ARPES). The second-order NLHE response under the THz field in the Hall rectification configuration is governed by an extrinsic contribution, which was determined by skew scattering and side-jump mechanisms of nontrivial topological surface states with opposite chirality and broken inversion symmetry. Our photodetectors based on 1T-$CoTe_2$ show a responsivity of 0.1 A W^{-1}, response time of 710 ns, and high signal-to-noise ratio at zero magnetic field.

2. Results

Bulk single crystals of 1T-$CoTe_2$ were grown via chemical vapor transport (CVT), as depicted in **Figure 1**a and described in the Experimental Section. Bulk $CoTe_2$ crystallizes in a CdI_2-type trigonal structure that belongs to the space group of $P\bar{3}m1$ (No. 164) and was confirmed by X-ray diffraction (XRD) (Figure S1, Supporting Information). The atomic arrangement of 1T-$CoTe_2$ implies that one Co atom is surrounded by six Te atoms (Figure 1b). Figure 1c shows a high-resolution transmission electron microscopy (HRTEM) image of a $CoTe_2$ few-layer cross-section that was prepared by focused ion beam technology along the [110] direction to obtain atomic information on the surface and bulk. The selected-area electron diffraction pattern indicates the excellent crystallinity shown in Figure 1d and Figure S1, Supporting Information. The spherical-aberration-corrected scanning transmission electron (STEM) microscopy images of the $CoTe_2$ nanosheets show that they are in the (010) plane, with lattice spacing of 3.48 Å and a (110) plane with lattice spacing of 2.0 Å (Figure 1e,f). Energy-dispersive spectroscopy analyses showed that the composition of Co:Te was 1:2 with regard to the atomic percentage. Elemental mapping (Figure 1g) shows that all the elements were distributed throughout the nanosheets. The surface of the nanosheets exposed to air assumes a native oxide skin with sub-nanometric thickness. To assess the environmental stability of bulk $CoTe_2$, the sample was directly exposed to air for different periods. The binding energies (BE) of Co-$2p_{3/2}$ and Te-$3d_{5/2}$ were 777.9 and 572.4 eV, respectively, as determined by X-ray photoemission spectroscopy (XPS) measurements as shown in Figure 1h.[20] The Co-2p doublet remains relatively unchanged after 1 h of air exposure, whereas the Te-3d doublet shows a new component at a BE of 575.9 eV ($J = 5/2$), which is consistent with Te—O.[21] The spectral weight of the new component of Te—O was only 7.5% of the total spectral area of the Te-3d core levels. Furthermore, after 1 year of air exposure, the Te—O component increased up to 12% of the total spectral area. In contrast

C.-N. Kuo, C. S. Lue
Department of Physics
Cheng Kung University
1 Ta-Hsueh Road, 70101, Tainan, Taiwan, China
X. Chen, W. Lu
School of Physical Science and Technology
ShanghaiTech University
Shanghai 201210, China

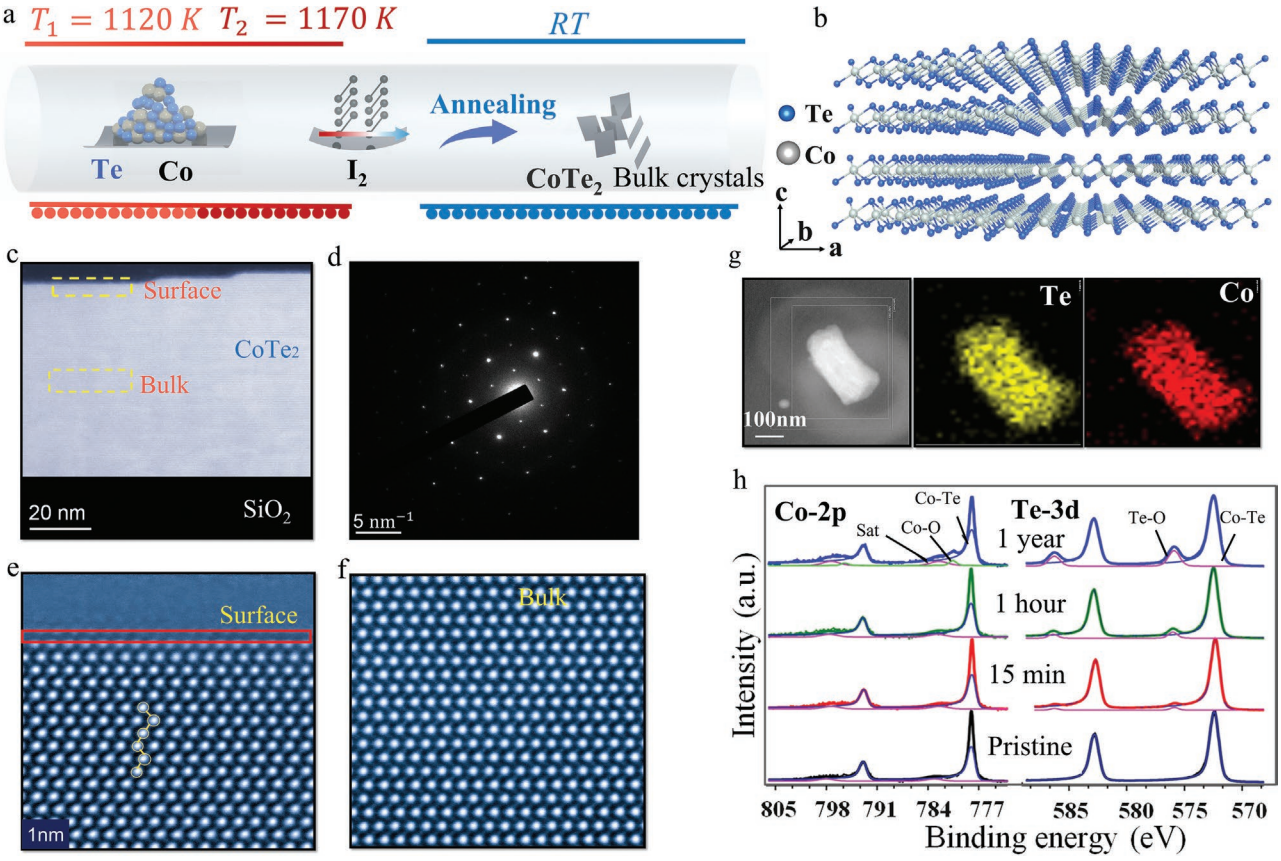

Figure 1. Growth and characterization of 1T-$CoTe_2$. a) Schematic illustration of the chemical vapor transport setup for synthesizing bulk $CoTe_2$ with Te powder, Co powder, and I_2 as precursors. b) Atomic structure of the $CoTe_2$ flake. The gray and blue spheres denote Co and Te atoms, respectively. c) HRTEM image of the layered $CoTe_2$ crystal. The scale bar is 20 nm. d) Selected-area electron diffraction patterns captured from the bulk area. e,f) Zoomed-in atomic-resolution spherical-aberration-corrected STEM images of the surface (e) and bulk (f) parts from (c), respectively. g) Low-magnified resolution transmission electron microscopy (TEM) image of a hexagonal 1T-$CoTe_2$ flake and energy-dispersive spectroscopy mapping of Co and Te elements. The scale bar is 100 nm. h) Co-2p and Te-3d core levels measured by X-ray photoemission spectroscopy experiments for the as-cleaved surface of $CoTe_2$ and its modification after air exposure at different times. The photon energy is 1486.6 eV (Al K_α) and all spectra were normalized to the maxima.

to the effect of short exposure to air, 1 year of air exposure induced the formation of a new component in the Co-2p spectra. The new component is recorded at a BE of 780.5 eV (for the $J=3/2$ component) and is ascribed to the formation of Co—O (3% of the total spectral area).[20b,22] Furthermore, from the XPS spectrum of $CoTe_2$ exposed to air for 1 year, the oxide layer is evidently a surface passivation layer, in which natural and spontaneous passivation acts to make the layer a self-assembled capping layer. Thus, the transport properties of the bulk crystal remained unchanged and were preserved over time. (The calculation of the oxide layer thickness is presented in Note S1, Supporting Information).

To study the second-order response at the microwave and THz frequencies, we used a second-harmonic generation (SHG) experiment to determine the symmetry of the material. SHG, including the second-order NLHE, exhibits periodically oscillating fields with a frequency twice that of the driving alternating current (2ω) and is accompanied by another direct current component that is generated by rectification. We performed SHG measurements using femtosecond laser pumping technology, as schematically depicted in **Figure 2**a. A comparative measurement of the SHG from $CoTe_2$ (blue line) and the mica substrate (red line) was conducted under 860 nm illumination and the significant reflected signal (430 nm) of the $CoTe_2$ sample is shown in Figure 2b. Because $CoTe_2$ is centrosymmetric in the bulk, the observation of an SHG signal indicates symmetry breaking at the surface. Notably, the surface states in a pristine crystal have the symmetry of the C_{3v} point group and lack an inversion center. The polarization-dependent second-harmonic signal in Figure 2c (tuned by a linear polarizer (Thorlabs LPVIS050) and a half waveplate (Thorlabs AHWP05M-980)) indicates strong anisotropy due to inversion symmetry breaking.

Next, the existence of spin-polarized surface states in $CoTe_2$ was demonstrated via density functional theory calculations and spin-ARPES experiments (Figures S2 and S3, Supporting Information). The presence of type-II Dirac fermions in bulk $CoTe_2$ (along with several other band inversions) was inferred from the presence of topologically protected surface states with time-reversal symmetry. The orbital-resolved band structure along the Γ–A direction (Figure 2d) with the irreducible representations of the bands indicates that the Dirac band crossing is composed of Te-5p orbitals, namely Te-p_x, Te-p_y, and Te-p_z orbitals, which also contributes to multiple band-inversion

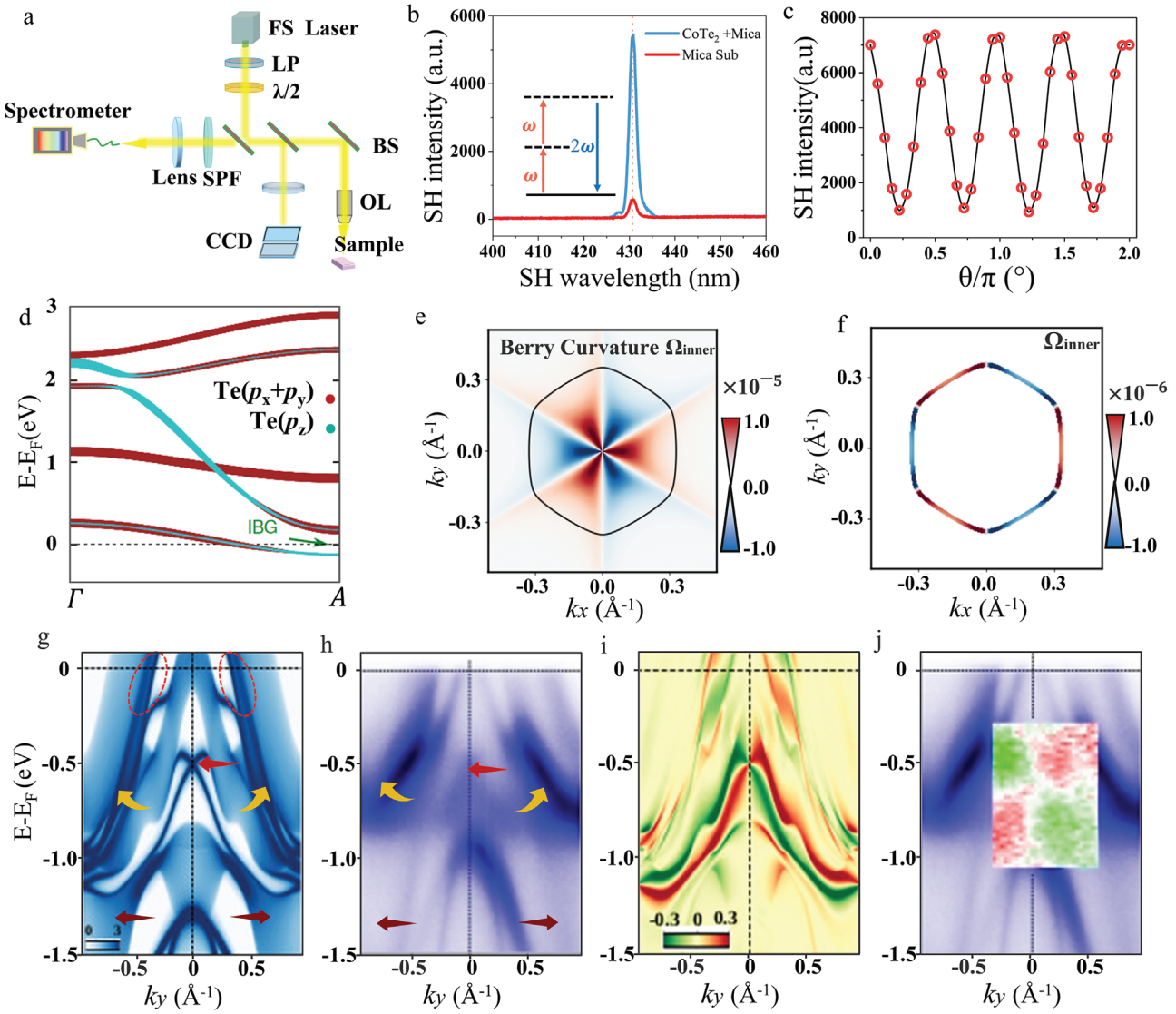

Figure 2. Second-harmonic generation (SHG) measurements without magnetic field, Berry curvature distribution, and spin- and angle-resolved photoelectron spectroscopy (spin-ARPES) measurements. a) Schematic of the SHG measurement setup. FS LASER, LP, $\lambda/2$, BS, SPF, and OL respectively represent femtosecond laser, linear polarizer, half-wave plate, beam splitter, short-pass filter, and objective lens. b) Measured spectra of the SHG from $CoTe_2$ (blue curve) and the mica substrate (red curve). c) Dependence of SHG emission on the polarization of the pumping laser. d) Orbital resolved bulk band dispersion of $CoTe_2$ along the Γ–A direction. The nontrivial band dispersions between the Te(p_x + p_y) and Te(p_z) orbitals in the conduction band, which gives rise to the surface states at the Fermi energy, are shown within the black dashed box. e) Schematic of the calculated Berry curvature distribution of the topological surface states on the whole Brillouin zone. The blue and red represent the negative and positive values of the Berry curvature, respectively. f) The calculated Berry curvature distribution over the Fermi surface. g) Density functional theory calculated momentum resolved spectral function plots along the $\overline{M}-\overline{\Gamma}-\overline{M}$ direction. The surface states near the Fermi energy are indicated by the red dashed lines and they originate from the topological bulk band inversion in the conduction band. h) Experimental ARPES spectra along the $\overline{M}-\overline{\Gamma}-\overline{M}$ direction of the (001) surface Brillouin zone. i,j) The calculated and experimental (measured by spin-ARPES) spin texture of the surface bands along the $\overline{M}-\overline{\Gamma}-\overline{M}$ direction.

gaps. To describe the origin of the Dirac band crossing in $CoTe_2$, the evolution of the p-orbital manifold of the Te atoms is reported in Figure S2, Supporting Information. Together, these orbitals give rise to several topologically protected surface states over a wide energy range in $CoTe_2$. The Berry curvature of wave functions can describe the bending of parameter spaces, including real space, momentum space, and any vector fields, owing to the geometry of the quantum eigenstates. The Berry curvature dipole, as the dipole moment of the Berry curvature in momentum space, is regarded as an effective magnetic field in momentum space, which is deeply connected to the NLHE. However, considering the threefold rotational symmetry of the topological surface state in $CoTe_2$, the Berry curvature dipole mechanism can be excluded owing to the opposite sign along the high-symmetry direction in Figure 2e,f.

The momentum-resolved spectral density plots along the $\overline{K}-\overline{\Gamma}-\overline{K}$ (Figure S3, Supporting Information) and $\overline{M}-\overline{\Gamma}-\overline{M}$ (Figure 2g) directions, along with the ARPES measurements (Figure 2h), capture the features of the bulk bands along with the surface states. There is a set of surface states at the Fermi

energy in Figure 2g–i, which arises from a bulk topological band inversion in the conduction band (Figure 2d). However, the surface states curve down and cross the Fermi energy, forming a pair of Rashba-like bands with a hexagonal Fermi surface at the Fermi energy (Figure S3d, Supporting Information). The presence of multiple additional topological bulk band inversions, one of which is marked by an arrow in Figure 2h, gives rise to nontrivial surface states along the $\overline{\mathrm{M}}-\overline{\Gamma}-\overline{\mathrm{M}}$ path, followed by the distribution of a pair of sharp hexagonal surface Fermi arc states around the $\overline{\Gamma}$ point. The consistency of the experimental and theoretical results confirms the presence of a bulk Dirac cone at an energy 0.49 eV below the Fermi energy. To further explore the spin polarization of the topological surface states, we also performed spin-polarized ARPES experiments along the $\overline{\mathrm{K}}-\overline{\Gamma}-\overline{\mathrm{K}}$ and $\overline{\mathrm{M}}-\overline{\Gamma}-\overline{\mathrm{M}}$ (Figure S3, Supporting Information) paths, with the component of the probed spin chosen as perpendicular to the direction of the dispersion. The corresponding calculated spin-resolved spectral function is shown in Figure 2i, where the crossings of the up- and down-spin bands are clearly observed, which is consistent with the measured spin polarization in Figure 2j. The spin-ARPES results indicate that the spin–momentum locking with time-reversal symmetry [$E_\sigma(k) = E_{-\sigma}(-k)$] is preserved, similar to the topological surface states.[23]

For the proof-of-concept illustration of a Hall rectifier, homogeneous $CoTe_2$ flakes are crossly contacted by a bow-tie-type antenna, following standard lithography and lift-off processes (Experimental Section). The photoresponse of the topological semimetal 1T-$CoTe_2$ at a low energy frequency stems from the intraband transitions, involving only carriers near the Fermi surface. To efficiently segregate the signal from background noise, a rectified structure with two additional electrodes transverse to the antenna is designed; the antenna can improve the sensitivity and collection efficiency of power from external radiation (**Figure 3**a). In such a setup, both longitudinal and transverse currents can be collected to distinguish the nonlinear response process described by the topological character of the Bloch wave functions. The oscillating THz-field enhanced by the bow-tie antenna induced a direct current along the transverse direction via a second-order NLHE response. In inversion-symmetry-breaking quantum materials, the rectification of the incident electric field at radio frequency is due to the contribution of a Berry curvature dipole. The Berry curvature is defined by $<\mathbf{\Omega}\mathrm{k} = \nabla_\mathrm{k} \times \mathbf{A(k)}>$[16b,24] and in centrosymmetric systems, $\mathbf{\Omega}\mathrm{k} = \mathbf{\Omega}–\mathbf{k}$ and $\mathbf{\Omega}\mathrm{k} = –\mathbf{\Omega}–\mathbf{k}$ under time-reversal symmetry. In our rectification process, the nonlinear response is governed by the nonlinear susceptibility tensor χ_{xyz}, whose values depend on the inversion symmetry (P) or time-reversal symmetry (T) breaking. In this regard, the nonlinear response function of the quantum wavefunction in $CoTe_2$ is influenced by the deep connection between the band topology and crystal symmetries.

The NHLE can be induced by intrinsic and extrinsic contributions, where the intrinsic contribution is dependent on the Berry curvature and the extrinsic contribution is determined by skew scattering and side-jump mechanisms.[25] However, second-order NLHE signals can still arise from extrinsic effects, such as skew scattering (called ballistic contribution) and side jump mechanisms.[26] That the existence of surface states near the Fermi energy results from bulk topological band inversion was confirmed using spin-ARPES in $CoTe_2$, as shown in Figure 2g–j. To highlight the role of surface states in generating the NLHE signal, we first note that the point-group symmetry of the bulk crystal $CoTe_2$ is time-reversal and inversion symmetry. Because of this, the bulk states cannot generate a second-order nonlinear response, whereas the threefold rotational crystal symmetry (C_{3v}) of the surface states in $CoTe_2$ lacks inversion symmetry, which meets the prerequisites for the NHLE. The experiments only probe the top surface of the $CoTe_2$ sample; hence, it is very likely that all second-order nonlinear responses arise from the surface states. Motivated by this, for THz detection experiments with low photon energy excitation, we attribute the observed signal to the surface states, in which the electron transport process is mainly performed at the topologically protected dissipationless surface states. Thus, for our device, we hypothesize that disorder-induced extrinsic skew scattering and side-jump mechanisms originate from the NLHE. The skew scattering process, resulting from transverse asymmetric scattering by effective spin–orbit coupling of the electron or impurity, plays a role in the transverse photoresponse of a Hall rectifier in the absence of the Berry curvature dipole. The side jump process that produces an anomalous distribution or velocity driven by the transverse displacement $\delta\mathbf{r}$ also contributes to the transverse photoresponse, as shown in Figure 3b. The second-order photoresponse is quadratically proportional to the incident electric field, as shown in Figure 3c (oscillating frequency ω). It can be expressed as $<J_\mathrm{a} = \sigma^{(3)}_{\mathrm{abc}} E_\mathrm{b} E_\mathrm{c}(\omega)>$, where J is the transverse current density and $\sigma^{(3)}_{\mathrm{abc}}$ is the C_{3v} symmetric crystal. According to the semiclassical Boltzmann transport theory calculation,[27] the second-order response of the topological surface state in non-centrosymmetric materials is described by $<J_{2,\mathrm{a}} = -e\int v_\mathrm{k}(k) f(k)>$, where the group velocity $<v_\mathrm{k} = v_0 + \mathrm{v_{sj}}>$ contains energy-band dispersion v_0 without the Berry curvature $\mathbf{\Omega}\mathrm{k}$ and side-jump v_{sj} contribution. In addition, the distribution function term $<f = f_0 + f_{\mathrm{ss}} + f_{\mathrm{ad}}>$ contains the equilibrium distribution f, skew scattering f_{ss}, and an anomalous distribution f_{ad} contribution. These parameters contribute to the second-order conductivity. A scaling analysis, referring to the relation between the transverse and longitudinal conductivity $<\sigma^{\mathrm{tran}} \approx (\sigma^{\mathrm{long}})^\alpha>$ with α as the scaling factor, could further separate the intrinsic and extrinsic contributions of the NLHE and identify the microscopic origin of the NLHE. Through symmetry analyses, the intrinsic contribution from the Berry curvature dipole was excluded because of the threefold rotational crystal symmetry (C_{3v}) of the surface states in $CoTe_2$, which causes the total Berry curvature dipole to disappear. Thus, the role of disorder-induced extrinsic skew scattering and side-jump mechanisms in the NLHE is indicated in this specific case.

With this understanding, we further explore the room-temperature features of the nonlinear Hall rectifier without invoking any external electric or magnetic fields. The normally incident THz wave is collimated and focused onto a spot by two polymethyl pentene lenses with an effective focal length of 35 mm; the bow-tie-type antenna can collect weak THz radiation that locally enhances the electric field intensity at the channel. Meanwhile, the type-II Dirac nature in $CoTe_2$

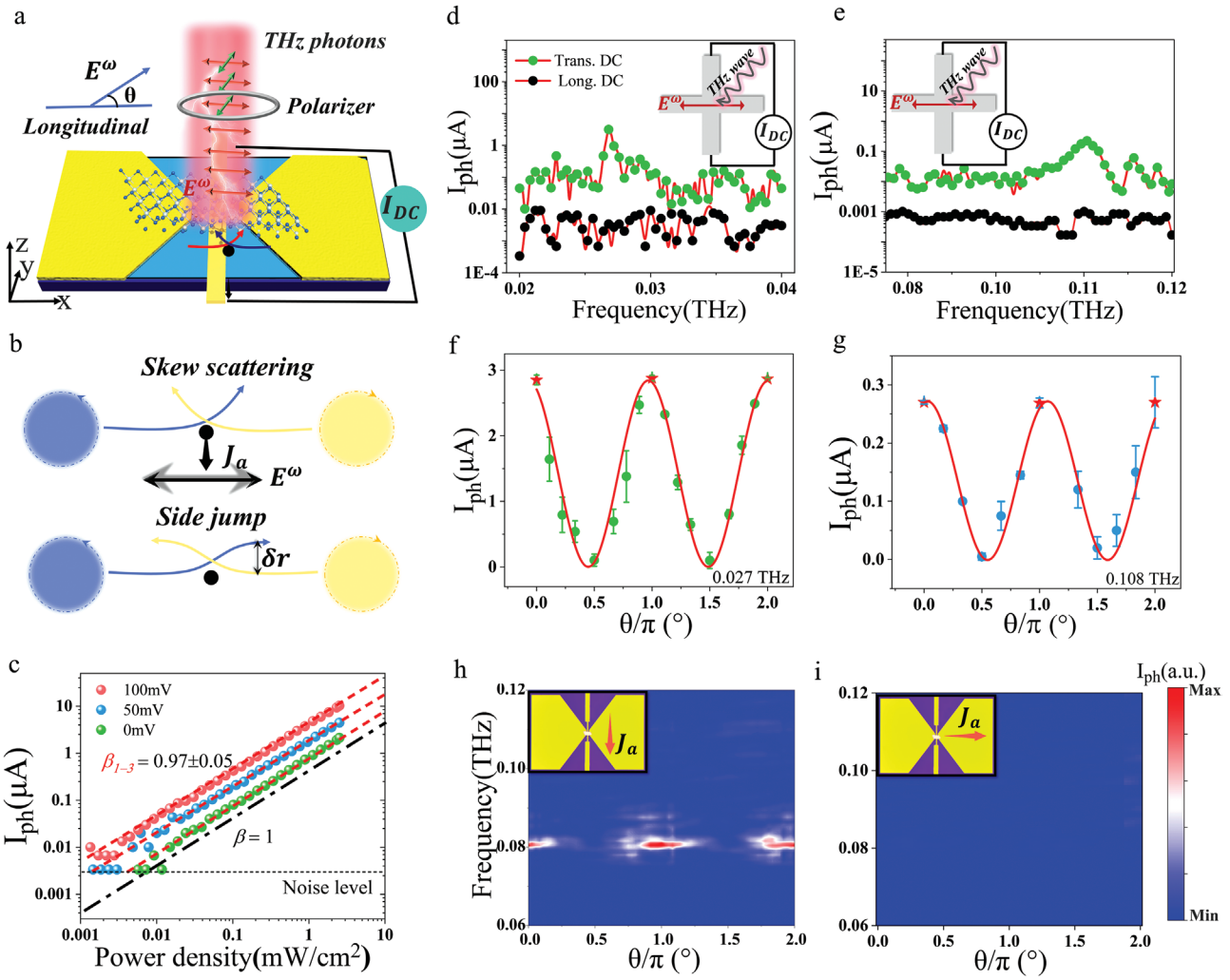

Figure 3. Terahertz detection of a 1T-$CoTe_2$-based nonlinear Hall rectifier. a) Schematic of the device architecture made from antenna-coupled Dirac semimetal $CoTe_2$. The oscillating terahertz electric field enhanced by the antenna induces a direct current in the transverse direction via the second-order nonlinear Hall response. b) Schematic of the skew scattering and side jump of topological surface states with opposite chiralities. c) Radiation power-dependent photocurrent in the $CoTe_2$ detector, suggesting a large linear dynamic range. The solid line is a fit to the data by $I_{ph} \approx P_{in}{}^{\beta}$ and $\alpha \approx 0.975$. d,e) The spectral dependence of the measured rectified photocurrent is obtained when the terahertz field is along the antenna ($\theta = 0°$). The inset shows the experimental geometry. Spectral frequency in 0.02–0.04 THz for (d), in 0.08–0.12 THz for (e). f,g) The polarization dependence of the transverse photocurrent, which reaches a maximum when the polarization angle $\theta = 0°$. The specific polarized optical current in (d) and (e) with peak frequencies of (f) 0.027 and (g) 0.108 THz, respectively. The possible origins of the experimental errors are as follows: i) the polarization angle has some ambiguity due to the influence of the polarizer frame and ii) the incidence angle of light to the detector may have small deviations, which has an impact on the experimental results. h,i) Color maps of the rectified photocurrent spectra along the longitudinal electrodes (h) and transverse electrodes (i) and at different polarization angles, which validates the NLHE character.

facilitates low-energy photon absorption owing to the presence of the type-II Dirac cone near the Fermi energy and topological surface states (TSS) near the Fermi energy. The transverse or longitudinal currents of the bulk states should be absent owing to the lack of inversion symmetry breaking. The important performance parameter of the THz detector is the dynamic range, which weighs the linearity of the photoresponse versus the varied incident power. Figure 3c shows the power dependence of our Hall rectifier by varying the excitation power from the lowest threshold at zero bias at 50 and 100 mV. Our detector exhibits ideal linearity over more than two orders of magnitude of optical power and the data are well fitted with a simple power law $<I_{ph} \propto P_{in}{}^{\beta}>$, with $\beta_1 = 0.97 \pm 0.005$ at room temperature and $\beta_2 = 0.97 \pm 0.005$ at 77 K. To further validate the photocurrent character of the $CoTe_2$ detector at 300 K, the dynamic photosignal curves with various incident radiation power were also recorded by an oscilloscope (Figure S10d, Supporting Information). The rectified photocurrent along the transverse direction (perpendicular to the antenna) was measured by varying the incident frequency (Figure 3d,e). In contrast, the longitudinal photosignal (along the direction of the antenna) is negligibly small, even though more radiation power can be collected by the antenna. Hall rectification can also be observed in devices by replacing the antenna arms with the same electrodes, similar to that along the transverse direction (Figures S5–S8, Supporting Information). By changing the polarization of the

THz wave, the sign of the signal remained unchanged and the maximum photocurrent was reached for the polarization angle θ oriented along the longitudinal direction, as shown in Figure 3f,g (color maps of polarization-resolved photoresponse are also shown in Figure 3h,i). These results agree well with the characteristics of the NLHE, substantiating the inherent nonlinearity of quantum materials and inversion breaking as the microscopic physical origins for the observed rectification. It is also clearly distinguished from NLHE-based room-temperature rectification due to the presence of Berry curvature in WSMs, which takes place only at several GHz[17a] or cryogenic temperatures[28] and vanishes at higher E_F values.[3b]

The rectification of topological surface states driven by intrinsic chirality in a single homogeneous material is unlimited by the thermal voltage threshold or transition time, which is innate to a semiconductor junction and much faster than the photothermal effects used in bolometers for thermal radiation detection. **Figure 4**a shows the timescale of the switchable signal under fast ON/OFF THz radiation modulation, which was output with a rise/fall time of 300 ns during the measurement. Rise and fall times of approximately 710 and 770 ns are derived for our Hall rectifier, corresponding to a 1.4 MHz electrical bandwidth (Figure S7, Supporting Information). Furthermore, the spectral response is characterized by varying the radiation frequencies over the range of 0.10–0.30 THz (Figure 4b). The fluctuation at lower frequencies is attributable to the reflection effect from the substrate or electric dipole effect from the antenna. Benefiting from the disorder-induced extrinsic skew scattering and side-jump mechanisms, which depend on the intrinsic material properties and intraband process, a broader spectral response is expected by incorporating a more advanced antenna with stronger optical-field coupling.

The achieved zero-bias responsivity of 0.1 A W^{-1} ($<R_A = I_{ph}/P_{in}\ S_\lambda>$, where the diffraction-limited area S_λ is larger than the active area S_a of the whole device) is unquestionably competitive with state-of-art detectors working at room temperature. The sensitivity of the $CoTe_2$-based Hall rectifier can be further evaluated by noise equivalent power (NEP) at 300 K, which is defined as the ratio between the noise density and responsivity. It represents the minimum detectable power with a unity signal-to-noise ratio in a 1 Hz bandwidth. Noise spectral density is measured without external bias at room temperature, as shown in Figure 4c, in which flicker noise ($1/f$ noise) dominates in the low-frequency range (below 1 kHz) owing to the fluctuation of electronic states, while white noise (including shot noise i_b and Johnson–Nyquist noise i_t) is the main contributor to the noise at higher frequencies. Shot noise, arising from the random generation and uncorrelated arrival of carriers, is evaluated by $<i_b^2 = 2qI_d/r_0>$, where q represents the electron charge, I_d is the bias current, and r_0 is the device resistance, which can be ignored because our device works without external bias. Johnson–Nyquist noise i_t is produced by the random thermal motion of charge carriers and is defined as $<i_t = 4k_BT/r_0>$, where k_B is the Boltzmann constant and T is the ambient temperature, which is of the same order of magnitude as the measurements. Following the aforementioned analysis, the optical NEP can reach less than 1 pW $Hz^{-1/2}$ without any external bias at ambient temperature (Figure 4d). The performance of our rectifier device is summarized in Figure 4e, reporting a peak responsivity of 0.4 A W^{-1}, maximum detectivity of 1×10^{12} Jones, and response time as fast as 700 ns. Additionally, the photocurrent can be improved by varying the bias voltage (Figure S9, Supporting Information) at the expense of an increased dark-current noise. By reducing the operating temperature to the liquid-nitrogen temperature (77 K), the thermal noise can be inhibited and the sensitivity of the $CoTe_2$ detector (Figure S10, Supporting Information) is improved by an order of magnitude. A comparison of detectors made from different low-dimensional materials and commercial detectors is provided in Figure 4f, which shows the superior performance of the Hall rectifier in terms of speed and sensitivity, even in its first implementation.[29]

To illustrate the practical application of our device, a transmissive imaging experiment was performed for non-destructive quality control. As a test object, abbreviation letters "U", "C", "A", and "S" (University of Chinese Academy of Sciences) made from copper foil and hidden inside a cardboard are used. To identify specific features of an object, a 0.30 THz radiation source is utilized and focused onto the Hall rectifier at the focal plane. During this process, the transmitted power after it is focused on the object is recorded without any bias voltage. A high-resolution image comprising 100×100 pixels (the integration time of each pixel is 20 ms) is reported in Figure 4e, clearly revealing the "UCAS" metallic letters with a high signal-to-noise ratio. These results represent a crucial milestone in the roadmap of Hall-rectifier-based science and technology. This study provides means to devise geometries, enabling appropriate engineering of the nonlinear electrical and optical properties of emerging topological semimetals with strong spin polarization to address targeted high-frequency application requirements.

3. Conclusion

We have reported the synthesis of a type-II Dirac semimetal candidate 1T-$CoTe_2$ with good crystallinity via the CVT route, which hosted strong spin–orbit coupling and nontrivial topologically-protected surface and bulk bands, as revealed by spin-ARPES and spectral function theory. A nonlinear THz photoresponse based on a second-order nonlinear Hall rectifier was generated from the extrinsic skew scattering and side-jump mechanisms of spin-textured chiral surface states under time-reversal symmetry at room temperature, without invoking any semiconductor junctions or Berry-curvature dipoles. Even in its first implementation, the THz nonlinear Hall rectifier showed a superb performance in terms of speed, sensitivity, and bandwidth. Our results open up fascinating prospects not only for advancing the fundamental-level understanding of topological physics but also for providing a novel strategy for overcoming the limitations of infrared/THz photonics by exploring the NLHE in newly emerging topological quantum materials.

4. Experimental Section

Growth Method: Single crystals of $CoTe_2$ were grown by the Te flux method.[30] Mixtures of high-purity Co powder (99.99%) and Te ingots (99.9999%) were sealed under vacuum in a quartz tube with a flat bottom. The quartz ampule was heated to 1320 K for 10 h and then

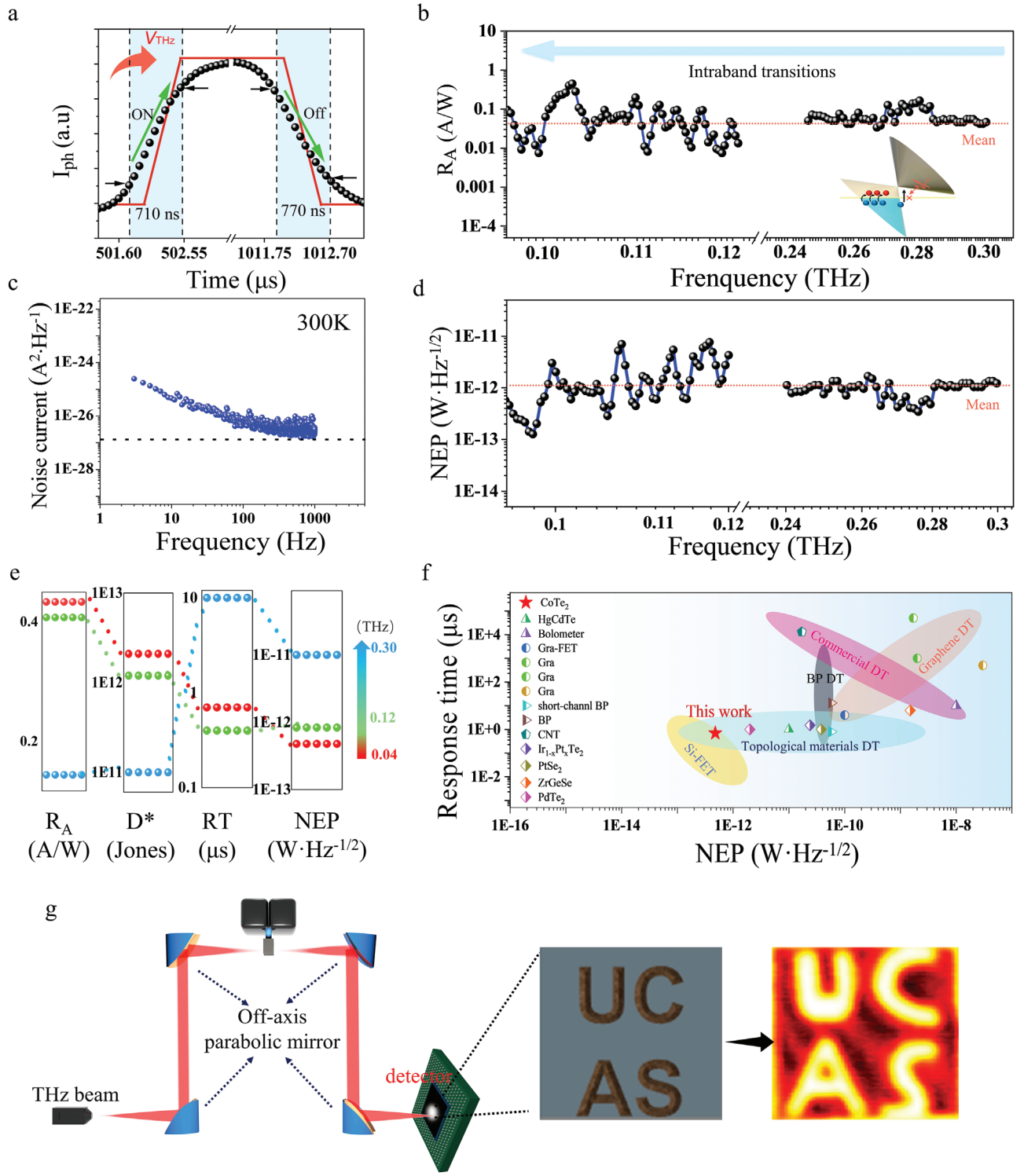

Figure 4. Systematic performance characterization and imaging applications of a $CoTe_2$-based Hall rectifier. a) Response electrical bandwidth of the $CoTe_2$ detector. b) Spectral responsivity as a function of the frequency at room temperature, without invoking external bias. The photon energy is in the range of 0.41–1.24 meV. c) Measured noise spectral density of the $CoTe_2$ detector at 300 K. d) Noise equivalent power (NEP) at 300 K, obtained as $N_I/|R_A|$. e) Responsivity, detectivity, NEP, and response time of the $CoTe_2$ detector at 300 K. f) Performance comparison of different terahertz detectors. g) Setup for terahertz imaging experiment. Four capital letters "UCAS" made from Cu foil were used as test objects and the incident power of 0.3 THz after beam focusing on the object was recorded by the Hall rectifier. The objects were clearly revealed in a cardboard envelope, which was invisible to the naked eye.

slowly cooled to 870 K at a rate of 3 K h^{-1}. Several shiny plate-like single crystals with typical sizes of 4 mm × 4 mm × 1 mm were harvested. The flat surface of the crystal corresponded to the (001) plane.

Characterizations: XPS experiments were performed using a monochromated Al-K_α X-ray source with a Specs Phoibos 150 multichannel electron energy analyzer. TEM characterization was performed by the JEM-F200 from Shanghai WEIPU Testing Technology Group Co., LTD.

Second-Harmonic Generation Measurements: SHG measurements were performed using the homemade microscopy system. The fundamental laser field was provided by an Nd:KGW laser at a wavelength of 860 nm with a pulse width of approximately 221 fs and a repetition rate of 1 MHz. The pulse laser was focused to a spot size of approximately 2 µm on the sample at a normal incidence by an Olympus microscope objective (50×, numerical aperture (NA) = 0.5) with a fixed linear polarization in the plane of the sample. The reflected SHG signal (430 nm) of the sample was collected using the same microscope objective and then fed into a spectrometer (SpectraPro HRS-500) equipped with a cooled charge-coupled device. To determine the dependence of the SHG emission on the polarization of the pumping laser measurement, the polarization direction of the fundamental wave was tuned using a linear polarizer (Thorlabs LPVIS050) and a half waveplate (Thorlabs AHWP05M-980) with a rotational step of 10°.

Device Fabrication: The $CoTe_2$ bulk crystal was mechanically exfoliated into nanosheets by blue tape and transferred onto a high-resistance silicon substrate with a 300 nm insulating layer of SiO_2 , in which silicon substrate purchased from Shanghai Onway Technology Co., Ltd. A standard ultraviolet lithography method was used to prepare the bow-tie-type antenna electrode pattern. Subsequently, metal contacts (Cr/Au = 15 nm/45 nm) were deposited by electron beam evaporation, after which they underwent a lift-off process to complete the device configuration. The fabrication method of the four-terminal antenna device followed the same procedure.

Device Characterizations: The electrical properties of the devices were measured using a digital source meter analyzer (Agilent B2912A) at room temperature (300 K). For photoresponse testing of the device, a W-band power amplifier connected to a Virginia Diodes Inc. (VDI) tripler (WR 2.8) was used to generate radiation in the range of 0.25–0.3 THz. In addition, a microwave source (Agilent E8257D) was connected to a VDI multiplier (WR 9.0) to generate radiation in the range of 0.07–0.12 THz. The output power of the THz radiation was calibrated using a TK100 power meter. The photodetector responsivity (R_A) was extracted from I_{ph} using the relation $R_A = I_{ph}/P_{in}$, where I_{ph} is the photocurrent recorded by the oscilloscope after the lock-in amplifier and low-noise voltage preamplifier and P is the incident photocurrent density ($P = P_{in}S_a$). Moreover, S_a is the effective area, which is 2.8×10^4 µm^2 for the device and much smaller than the diffraction-limited area $S_\lambda = \lambda^2/4$ of 0.04, 0.12, and 0.3 THz. P_{in} is the power density (1 mW cm^{-2} at 0.3 THz). The NEP was one of the figures of merit used to evaluate devices, corresponding to the minimum detectable power with a 1 Hz bandwidth. This was given by NEP = ν_n /R_v, where ν_n, R_v ($R_v = r \times R_A$), and r represent the root mean square of the noise voltage, voltage responsivity, and resistance, respectively. Furthermore, $\nu_n = (\nu_t^2 + v_s^2)^{1/2} = (4k_BTr + 2eI_dr^2)^{1/2}$, ν_t and ν_s represent the thermal Johnson–Nyquist and shot noise, respectively, k_B is the Boltzmann constant, T is the ambient temperature, e is the elementary charge, and I_d is the bias current.

Supporting Information

Supporting Information is available from the Wiley Online Library or from the author.

Acknowledgements

This work was supported by the National Key R&D Program of China (No. 2021 YFB2800700), the National Natural Science Foundation of China (No. 61 521 005, 61 875 217, 91 850 208, 62 005 249), and STCSM Grants (No. 1 859 078 100, 19 590 780 100). This project was funded by the State Key Laboratory for Modification of Chemical Fibres and Polymer Materials, Donghua University (KF1809). Shanghai Municipal Science and Technology Major Project (Grant No. 2019SHZDZX01). Science and Technology Commission of Shanghai Municipality (21ZR1473800). Sponsored by Zhejiang Lab (2021MB0AB01). The Zhejiang Provincial Natural Science Foundation (LQ20F050005) and Excellent Postdoctoral Research Projects of Zhejiang Province (ZJ2021019). C acknowledges the Science and Engineering Research Board (SERB), India, for financial support under the National Postdoctoral Fellowship (PDF/2021/000346). The authors would like to thank the Science and Engineering Research Board (for MTR/2019/0 01520) and the Department of Science and Technology (DST, for Project DST/NM/TUE/QM- 6/2019(G)-IIT Kanpur) of the Government of India for their financial support. D.F. acknowledges the Spanish Ministerio de Ciencia e Innovación under Project No. PID2019–109525RB-I00. D.F. acknowledges financial support from the Spanish Ministry of Economy and Competitiveness through the "María de Maeztu" Program for Units of Excellence in R&D (No. CEX2018-000805-M). D.F. also acknowledges the EU's H2020 framework program for research and innovation under grant agreements NFFA-Europe (n. 654 360 from 1/9/2015 to 28/02/2021) and NFFA-Europe-Pilot (n. 101 007 417 from 1/03/2021 to 28/02/2026) for access to TEM.

Open Access Funding provided by Universita degli Studi dell'Aquila within the CRUI-CARE Agreement.

Conflict of Interest

The authors declare no conflict of interest.

Author Contributions

Z.H. and L.Z. contributed equally to this work. L.B.Z., L.W., and Z.H. wrote the manuscript, with the support of A.P., A.A., A.C., and B.G. for parts related to physicochemical and electronic properties. L.W., X.S.C., and W.L. supervised the project and discussed experimental results. The growth of bulk $CoTe_2$ materials was done by B.G. and D.F. Z.H. fabricated all devices and performed all photoresponse measurements. L.B.Z., K.X.Z., Z.Q.Z.C., and C.Y.Y. provided effective measurement ideas and some test conditions. L.H. simulated antennas. A.P.G. performed AFM characterization and SHG measurements. Y.C.Z. and W.D.H. performed the noise spectrum measurements. A.A. and A.C. conducted first-principles calculations. ARPES experiments were performed by J.F., A.P., and I.V. All authors commented on and discussed this work.

Data Availability Statement

The data that support the findings of this study are available from the corresponding author upon reasonable request.

Keywords

1T-$CoTe_2$, nonlinear Hall effect, terahertz rectification, type-II Dirac semimetals

Received: October 17, 2022
Revised: January 4, 2023
Published online: January 22, 2023

[1] a) T. R. Chang, S. Y. Xu, D. S. Sanchez, W. F. Tsai, S. M. Huang, G. Chang, C. H. Hsu, G. Bian, I. Belopolski, Z. M. Yu, S. A. Yang,

T. Neupert, H. T. Jeng, H. Lin, M. Z. Hasan, *Phys. Rev. Lett.* **2017**, *119*, 026404; b) P. Liu, J. R. Williams, J. J. Cha, *Nat. Rev. Mater.* **2019**, *4*, 479; c) J. E. Moore, *Nature* **2010**, *464*, 194; d) A. Q. Wang, X. G. Ye, D. P. Yu, Z. M. Liao, *ACS Nano* **2020**, *14*, 3755.

[2] a) M. Yan, H. Huang, K. Zhang, E. Wang, W. Yao, K. Deng, G. Wan, H. Zhang, M. Arita, H. Yang, Z. Sun, H. Yao, Y. Wu, S. Fan, W. Duan, S. Zhou, *Nat. Commun.* **2017**, *8*, 257; b) A. A. Soluyanov, D. Gresch, Z. Wang, Q. Wu, M. Troyer, X. Dai, B. A. Bernevig, *Nature* **2015**, *527*, 495.

[3] a) Z. Z. Du, H.-Z. Lu, X. C. Xie, *Nat. Rev. Phys.* **2021**, *3*, 744; b) Z. Z. Du, C. M. Wang, S. Li, H. Z. Lu, X. C. Xie, *Nat. Commun.* **2019**, *10*, 3047.

[4] a) Q. Ma, S.-Y. Xu, C.-K. Chan, C.-L. Zhang, G. Chang, Y. Lin, W. Xie, T. Palacios, H. Lin, S. Jia, P. A. Lee, P. Jarillo-Herrero, N. Gedik, *Nat. Phys.* **2017**, *13*, 842; b) J. Ma, K. Deng, L. Zheng, S. Wu, Z. Liu, S. Zhou, D. Sun, *2D Mater.* **2019**, *6*, 032001.

[5] S. Kovalev, R. M. A. Dantas, S. Germanskiy, J. C. Deinert, B. Green, I. Ilyakov, N. Awari, M. Chen, M. Bawatna, J. Ling, F. Xiu, P. H. M. van Loosdrecht, P. Surowka, T. Oka, Z. Wang, *Nat. Commun.* **2020**, *11*, 2451.

[6] E. Javadi, D. B. But, K. Ikamas, J. Zdanevicius, W. Knap, A. Lisauskas, *Sensors* **2021**, *21*, 2909.

[7] T. Morimoto, N. Nagaosa, *Sci. Adv.* **2016**, *2*, e1501524.

[8] Q. Ma, A. G. Grushin, K. S. Burch, *Nat. Mater.* **2021**, *20*, 1601.

[9] J. Zhang, T. Zhang, L. Yan, C. Zhu, W. Shen, C. Hu, H. Lei, H. Luo, D. Zhang, F. Liu, Z. Liu, J. Tong, L. Zhou, P. Yu, G. Yang, *Adv. Mater.* **2022**, *34*, 2204621.

[10] a) S. Dhara, E. Mele, R. Agarwal, *Science* **2015**, *349*, 726; b) J. Ma, B. Cheng, L. Li, Z. Fan, H. Mu, J. Lai, X. Song, D. Yang, J. Cheng, Z. Wang, C. Zeng, D. Sun, *Nat. Commun.* **2022**, *13*, 5425.

[11] Z. Ji, G. Liu, Z. Addison, W. Liu, P. Yu, H. Gao, Z. Liu, A. M. Rappe, C. L. Kane, E. J. Mele, R. Agarwal, *Nat. Mater.* **2019**, *18*, 955.

[12] H. Nyquist, *Phys. Rev.* **1928**, *32*, 110.

[13] a) M. Z. Hasan, G. Chang, I. Belopolski, G. Bian, S.-Y. Xu, J.-X. Yin, *Nat. Rev. Mater.* **2021**, *6*, 784; b) A. Thilagam, *Phys. Rev. B* **1998**, *59*, 3027.

[14] a) Q. Wang, J. Zheng, Y. He, J. Cao, X. Liu, M. Wang, J. Ma, J. Lai, H. Lu, S. Jia, D. Yan, Y. Shi, J. Duan, J. Han, W. Xiao, J. H. Chen, K. Sun, Y. Yao, D. Sun, *Nat. Commun.* **2019**, *10*, 5736; b) Z. Fei, T. Palomaki, S. Wu, W. Zhao, X. Cai, B. Sun, P. Nguyen, J. Finney, X. Xu, D. H. Cobden, *Nat. Phys.* **2017**, *13*, 677; c) M. S. Bahramy, O. J. Clark, B. J. Yang, J. Feng, L. Bawden, J. M. Riley, I. Markovic, F. Mazzola, V. Sunko, D. Biswas, S. P. Cooil, M. Jorge, J. W. Wells, M. Leandersson, T. Balasubramanian, J. Fujii, I. Vobornik, J. E. Rault, T. K. Kim, M. Hoesch, K. Okawa, M. Asakawa, T. Sasagawa, T. Eknapakul, W. Meevasana, P. D. C. King, *Nat. Mater.* **2018**, *17*, 21.

[15] a) A. Markou, J. M. Taylor, A. Kalache, P. Werner, S. S. P. Parkin, C. Felser, *Phys. Rev. Mater.* **2018**, *2*, 051001; b) H. C. Zhao, H. Xia, S. Hu, Y. Y. Lv, Z. R. Zhao, J. He, E. Liang, G. Ni, L. Y. Chen, X. P. Qiu, S. M. Zhou, H. B. Zhao, *Nat. Commun.* **2021**, *12*, 5266.

[16] a) C. Ortix, *Adv. Quantum Technol.* **2021**, *4*, 2100056; b) I. Sodemann, L. Fu, *Phys. Rev. Lett.* **2015**, *115*, 216806.

[17] a) D. Kumar, C. H. Hsu, R. Sharma, T. R. Chang, P. Yu, J. Wang, G. Eda, G. Liang, H. Yang, *Nat. Nano* **2021**, *16*, 421; b) Q. Ma, S. Y. Xu, H. Shen, D. MacNeill, V. Fatemi, T. R. Chang, A. M. Mier Valdivia, S. Wu, Z. Du, C. H. Hsu, S. Fang, Q. D. Gibson, K. Watanabe, T. Taniguchi, R. J. Cava, E. Kaxiras, H. Z. Lu, H. Lin, L. Fu, N. Gedik, P. Jarillo-Herrero, *Nature* **2019**, *565*, 337.

[18] P. He, H. Isobe, D. Zhu, C. H. Hsu, L. Fu, H. Yang, *Nat. Commun.* **2021**, *12*, 698.

[19] Y. Zhang, L. Fu, *Proc. Natl. Acad. Sci. U. S. A.* **2021**, *118*, e2100736118.

[20] a) X. Chia, Z. Sofer, J. Luxa, M. Pumera, *Chemistry* **2017**, *23*, 11719; b) D. V. Cesar, C. A. Peréz, M. Schmal, V. M. M. Salim, *Appl. Surf. Sci.* **2000**, *157*, 159; c) S. Nappini, D. W. Boukhvalov, G. D'Olimpio, L. Zhang, B. Ghosh, C. N. Kuo, H. Zhu, J. Cheng, M. Nardone, L. Ottaviano, *Adv. Funct. Mater.* **2020**, *30*, 2000915.

[21] O. A. Balitskii, W. Jaegermann, *Mater. Chem. Phys.* **2006**, *97*, 98.

[22] Z. Y. Tian, H. Vieker, P. M. Kouotou, A. Beyer, *Faraday Discuss.* **2015**, *177*, 249.

[23] B. Ghosh, D. Mondal, C.-N. Kuo, C. S. Lue, J. Nayak, J. Fujii, I. Vobornik, A. Politano, A. Agarwal, *Phys. Rev. B* **2019**, *100*, 195134.

[24] J. Ma, Q. Gu, Y. Liu, J. Lai, P. Yu, X. Zhuo, Z. Liu, J. H. Chen, J. Feng, D. Sun, *Nat. Mater.* **2019**, *18*, 476.

[25] Z. Z. Du, C. M. Wang, H. P. Sun, H. Z. Lu, X. C. Xie, *Nat. Commun.* **2021**, *12*, 5038.

[26] a) J. N. Chazalviel, *Phys. Rev. B* **1974**, *10*, 3018; b) M. M. Glazov, L. E. Golub, *Phys. Rev. Lett.* **2020**, *125*, 157403; c) C.-Z. Wang, H.-Y. Xu, Y.-C. Lai, *Phys. Rev. B* **2021**, *103*, 195439.

[27] a) S. Park, S. Woo, E. J. Mele, H. Min, *Phys. Rev. B* **2017**, *95*, 161113; b) H. Min, P. Jain, S. Adam, M. D. Stiles, *Phys. Rev. B* **2011**, *83*, 195117; c) S. Adam, P. W. Brouwer, S. Das Sarma, *Phys. Rev. B* **2009**, *79*, 201404.

[28] K. Kang, T. Li, E. Sohn, J. Shan, K. F. Mak, *Nat. Mater.* **2019**, *18*, 324.

[29] a) D. Spirito, D. Coquillat, S. L. D. Bonis, A. Lombardo, M. Bruna, A. C. Ferrari, V. Pellegrini, A. Tredicucci, W. Knap, M. S. Vitiello, *Appl. Phys. Lett.* **2014**, *104*, 061111; b) P. Crump, S. Boldicke, C. M. Schultz, H. Ekhteraei, H. Wenzel, G. Erbert, *Semicond. Sci. Technol.* **2012**, *27*, 045001; c) L. Vicarelli, M. S. Vitiello, D. Coquillat, A. Lombardo, A. C. Ferrari, W. Knap, M. Polini, V. Pellegrini, A. Tredicucci, *Nat. Mater.* **2012**, *11*, 865; d) J. Tong, M. Muthee, S. Y. Chen, S. K. Yngvesson, J. Yan, *Nano Lett.* **2015**, *15*, 5295; e) D. Suzuki, Y. Ochiai, Y. Kawano, *ACS Omega* **2018**, *3*, 3540; f) S. Castilla, B. Terres, M. Autore, L. Viti, J. Li, A. Y. Nikitin, I. Vangelidis, K. Watanabe, T. Taniguchi, E. Lidorikis, M. S. Vitiello, R. Hillenbrand, K. J. Tielrooij, F. H. L. Koppens, *Nano Lett.* **2019**, *19*, 2765; g) C. Guo, Y. Hu, G. Chen, D. Wei, L. Zhang, Z. Chen, W. Guo, H. Xu, C.-N. Kuo, C. S. Lue, X. Bo, X. Wan, L. Wang, A. Politano, X. Chen, W. Lu, *Sci. Adv.* **2020**, *6*, eabb6500; h) W. Guo, Z. Dong, Y. Xu, C. Liu, D. Wei, L. Zhang, X. Shi, C. Guo, H. Xu, G. Chen, L. Wang, K. Zhang, X. Chen, W. Lu, *Adv. Sci.* **2020**, *7*, 1902699; i) H. Xu, F. Fei, Z. Chen, X. Bo, Z. Sun, X. Wan, L. Han, L. Wang, K. Zhang, J. Zhang, G. Chen, C. Liu, W. Guo, L. Yang, D. Wei, F. Song, X. Chen, W. Lu, *ACS Nano* **2021**, *15*, 5138; j) L. Zhang, Z. Dong, L. Wang, Y. Hu, C. Guo, L. Guo, Y. Chen, L. Han, K. Zhang, S. Tian, C. Yao, Z. Chen, M. Cai, M. Jiang, H. Xing, X. Yu, X. Chen, K. Zhang, W. Lu, *Adv. Sci.* **2021**, *8*, 2102088; k) L. Wang, L. Han, W. Guo, L. Zhang, C. Yao, Z. Chen, Y. Chen, C. Guo, K. Zhang, C. N. Kuo, C. S. Lue, A. Politano, H. Xing, M. Jiang, X. Yu, X. Chen, W. Lu, *Light: Sci. Appl.* **2022**, *11*, 53.

[30] Y. Yoo, Z. P. DeGregorio, Y. Su, S. J. Koester, J. E. Johns, *Adv. Mater.* **2017**, *29*, 1605461.